Chirality dependence of exciton effects in single-wall carbon nanotubes: Tight-binding model

Chirality dependence of exciton effects in single-wall carbon nanotubes: Tight-binding model

J. Jiang,[1] R. Saito,[1] Ge. G. Samsonidze,[2] A. Jorio,[3] S. G. Chou,[4] G. Dresselhaus,[5] and M. S. Dresselhaus[2,6]

[1]*Department of Physics, Tohoku University and CREST JST, Sendai 980-8578, Japan*

[2]*Department of Electrical Engineering and Computer Science, Massachusetts Institute of Technology, Cambridge, Massachusetts 02139-4307, USA*

[3]*Departamento de Física, Universidade Federal de Minas Gerais, Belo Horizonte-MG, 30123-970 Brazil*

[4]*Pfizer Global Research and Development, Eastern Point Road, Groton, Connecticut 06340, USA*

[5]*Francis Bitter Magnet Laboratory, Massachusetts Institute of Technology, Cambridge, Massachusetts 02139-4307, USA*

[6]*Department of Physics, Massachusetts Institute of Technology, Cambridge, Massachusetts 02139-4307, USA*

We have studied the exciton properties of single-wall carbon nanotubes by solving the Bethe-Salpeter equation within tight-binding models. The screening effect of the π electrons in carbon nanotubes is treated within the random phase and static screened approximations. The exciton wave functions along the tube axis and circumference are discussed as a function of (n,m). A $2n+m=$const family behavior is found in the exciton wave function length, excitation energy, binding energy, and environmental shift. This family behavior is understood in terms of the trigonal warping effect around the K point of a graphene layer and curvature effects. The large family spread in the excitation energy of the Kataura plot is found to come from the single-particle energy.

　　　　　　　　PACS number(s): 78.67.Ch, 78.67.−n, 71.35.Cc

I. INTRODUCTION

Single wall carbon nanotube (SWNT) structures can be characterized by two integers (n,m) with $2n+m=3p+r$, where p is an integer and $r=0,1,2$ define metallic (M), semiconducting type I (SI), and type II (SII) SWNTs, respectively.[1–3] The synthesis and observation of the properties of SWNTs have advanced greatly in recent years, making possible the experimental study of the optical properties of individual SWNTs.[4–7] Advances in the measurements of the optical properties of individual SWNTs provided a wealth of information, but they also highlighted puzzles in our understanding of nanotubes.

In particular, the optical transition energies have been studied in a recent series of fluorescence and Raman spectroscopy experiments.[4,8,9] Though some aspects of the experiments can be interpreted within the context of a simple, noninteracting electron model,[2,3] it has become increasingly clear that electron-electron interactions also play an important role in determining the optical transition energies, e.g., the "ratio problem."[10] Moreover, both theoretical calculations and experimental measurements show that the exciton binding energies are anomalously large in nanotubes, corresponding to a substantial fraction of the band gap, indicating the importance of many-body effects in this quasi-one-dimensional system.[11–14] Furthermore, exciton relaxation processes have been studied in both the frequency and time domains.[15–19]

Within a static screened Hartree Fock approximation, Ando has studied excitations in nanotubes.[20] Recently, first-principles calculations of the effects of many-electron interactions on the optical properties were performed for nanotubes with a small diameter (d_t)[11,12,21,22] and there have also been some descriptions of excitons in nanotubes based on other models.[23–26] The systematic dependence of the transition energies on the nanotube radius has been addressed and the "ratio problem" has been solved.[10,27,28] The radiative life-

time of excitons in semiconducting SWNTs was estimated by both *ab initio*[22] and tight-binding[24] (TB) methods. The exciton binding energy E_{bd} was found to depend on the chiral angle (θ) via an effective mass m^* by $E_{bd} \propto (m^*)^{\alpha-1}$ with α an empirical parameter.[23] This formula is proper for SWNTs with d_t larger than 1.0 nm.[23] For SWNTs with a small diameter, the curvature effect also contributes to the chiral angle dependence of the exciton binding energy. In the present work, we found that the curvature effect modifies the detailed family patterns of the exciton binding energy by increasing the family spread in the small d_t range. Moreover, the systematic dependences of the excitation energy, the environment-induced energy shift, and the wave function size on the nanotube chiral angle have not been discussed previously. The wave function information of nanotubes is especially important for discussing their physical properties. For example, the chirality dependence of the wave function size is essential for explaining the chirality dependences of the exciton-photon and exciton-phonon matrix elements.[29] Furthermore, a Kataura plot based on an exciton picture has not been given previously. In this paper, we address these issues by a systematic study of the dependence of the excitonic properties on the nanotube chirality.

We study exciton effects within a TB approximation. The electron-hole corrections are included via the Bethe-Salpeter (BS) equation. The π electron screening effect is calculated within the random phase approximation (RPA) and a static screened approximation, which work well for nanotubes.[20,28] The systematic dependence of exciton effects on the SWNT chirality is addressed here, including results for E_{11}^M and E_{ii}^S ($i=1, 2, 3,$ and 4).

In Sec. II, we develop the method for calculating the exciton excitation spectra within the framework of the TB approximation. In Sec. III, we show the exciton wave functions along the tube axis and circumference. In Sec. IV, the excitation energy, binding energy, and excitation energy shift due to the environment are discussed and family patterns are

found in these spectra. The large family spread in the excitation energy Kataura plot is found to arise from the single-particle spectra. Discussions and a summary are given in Sec. V.

II. THEORETICAL METHOD

We calculate the coupled electron-hole excitation energies Ω_n and wave functions Ψ^n by solving the BS equation[11]

$$\{[E(\mathbf{k}_c) - E(\mathbf{k}_v)]\delta(\mathbf{k}'_c, \mathbf{k}_c)\delta(\mathbf{k}'_v, \mathbf{k}_v) + K(\mathbf{k}'_c\mathbf{k}'_v, \mathbf{k}_c\mathbf{k}_v)\}\Psi^n(\mathbf{k}_c\mathbf{k}_v)$$
$$= \Omega_n\Psi^n(\mathbf{k}'_c\mathbf{k}'_v), \tag{1}$$

where $\mathbf{k}_c$ and $\mathbf{k}_v$ denote wave vectors of the conduction and valence energy bands and $E(\mathbf{k}_c)$ and $E(\mathbf{k}_v)$ are the quasielectron and quasihole energies, respectively. Ω_n is the energy of the nth excitation, and $\Psi^n(\mathbf{k}_c\mathbf{k}_v)$ are the excitonic wave functions. The kernel $K(\mathbf{k}'_c\mathbf{k}'_v, \mathbf{k}_c\mathbf{k}_v)$ is given by

$$K(\mathbf{k}'_c\mathbf{k}'_v, \mathbf{k}_c\mathbf{k}_v) = 2\delta_S K^x(\mathbf{k}'_c\mathbf{k}'_v, \mathbf{k}_c\mathbf{k}_v) - K^d(\mathbf{k}'_c\mathbf{k}'_v, \mathbf{k}_c\mathbf{k}_v), \tag{2}$$

with $\delta_S = 1$ for spin singlet and 0 for spin triplet states. The direct and exchange terms K^d and K^x are given by the following integrals:[30]

$$K^d(\mathbf{k}'_c\mathbf{k}'_v, \mathbf{k}_c\mathbf{k}_v) = W(\mathbf{k}'_c\mathbf{k}_c, \mathbf{k}'_v\mathbf{k}_v)$$
$$= \int d\mathbf{r}' d\mathbf{r} \psi^*_{\mathbf{k}'_c}(\mathbf{r}')\psi_{\mathbf{k}_c}(\mathbf{r}')w(\mathbf{r}', \mathbf{r})$$
$$\times \psi_{\mathbf{k}'_v}(\mathbf{r})\psi^*_{\mathbf{k}_v}(\mathbf{r}),$$

$$K^x(\mathbf{k}'_c\mathbf{k}'_v, \mathbf{k}_c\mathbf{k}_v) = \int d\mathbf{r}' d\mathbf{r} \psi^*_{\mathbf{k}'_c}(\mathbf{r}')\psi_{\mathbf{k}'_v}(\mathbf{r}')v(\mathbf{r}', \mathbf{r})$$
$$\times \psi_{\mathbf{k}_c}(\mathbf{r})\psi^*_{\mathbf{k}_v}(\mathbf{r}), \tag{3}$$

with w and v the screened and bare Coulomb potentials, respectively, and ψ the quasi-particle eigenfunction as discussed below. In the above equation, we have introduced the screened Coulomb interaction W. The unscreened Coulomb interaction V can be defined by replacing w in W by v.

The quasiparticle energies are calculated by including the self-energy corrections

$$E(\mathbf{k}_c) = \epsilon(\mathbf{k}_c) + \Sigma(\mathbf{k}_c), \quad E(\mathbf{k}_v) = \epsilon(\mathbf{k}_v) + \Sigma(\mathbf{k}_v), \tag{4}$$

with $\epsilon(\mathbf{k})$ the single-particle energy and $\Sigma(\mathbf{k})$ the self-energy

$$\Sigma(\mathbf{k}_c) = -\sum_{\mathbf{q}} W[\mathbf{k}_c(\mathbf{k} + \mathbf{q})_v, (\mathbf{k} + \mathbf{q})_v\mathbf{k}_c],$$

$$\Sigma(\mathbf{k}_v) = -\sum_{\mathbf{q}} W[\mathbf{k}_v(\mathbf{k} + \mathbf{q})_v, (\mathbf{k} + \mathbf{q})_v\mathbf{k}_v]. \tag{5}$$

We consider the dielectric screening effect within the RPA. In the RPA, the static screened Coulomb interaction is expressed as[20]

$$W[(\mathbf{k}' + \mathbf{q})a_1\mathbf{k}'a_2, (\mathbf{k} + \mathbf{q})a_3\mathbf{k}a_4]$$
$$= V[(\mathbf{k}' + \mathbf{q})a_1\mathbf{k}'a_2, (\mathbf{k} + \mathbf{q})a_3\mathbf{k}a_4]/\kappa\epsilon(\mathbf{q}). \tag{6}$$

Here $a = c, v$, and κ is a static dielectric constant describing

the effects of electrons in core states, σ bands, and surrounding materials. In Eq. (6), an effective screening has been expressed as a product of the dielectric function for π electrons $\epsilon(\mathbf{q})$ and the dielectric constant for the core states, σ bands, and the surrounding environment. The reasons are as follows. The Coulomb interaction in a media with a dielectric constant κ is expressed as $V(\mathbf{q})/\kappa$. When we further consider the screening effect from electrons, the interaction $V(\mathbf{q})/\kappa$ is reduced and under the RPA, it is scaled by a dielectric function $1/\epsilon(\mathbf{q})$, i.e., $[V(\mathbf{q})/\kappa]/\epsilon(\mathbf{q}) = V(\mathbf{q})/\kappa\epsilon(\mathbf{q})$. In this paper, the screening effects from the core states, σ bands are also included in κ. The same effective Coulomb interaction as in Eq. (6) has been used in previous studies and it was found that it works well in carbon nanotubes.[20,27,28] We take $\kappa = 2$ in this paper unless otherwise mentioned. The calculated binding energies with $\kappa = 2$ for the exciton associated with the second allowed transition in (10, 3) and (7, 5) SWNTs are 0.55 and 0.58 eV, respectively, and these values agree well with those found by experiment, i.e., (0.49 ± 0.05) eV and (0.62 ± 0.05) eV.[31] In Eq. (6), $\epsilon(\mathbf{q})$ is the dielectric function describing effects of the polarization of the π bands[20]

$$\epsilon(\mathbf{q}) = 1 + v(\mathbf{q})\Pi(\mathbf{q}). \tag{7}$$

The polarization Π in Eq. (7) is given by[32]

$$\Pi(\mathbf{q}) = -2 \sum_{\mathbf{k}aa'} \frac{f_{\mathbf{k}+\mathbf{q}a'} - f_{\mathbf{k}a}}{\epsilon_{\mathbf{k}+\mathbf{q}a'} - \epsilon_{\mathbf{k}a}} \left| \int \psi^*_{\mathbf{k}a}(\mathbf{r})e^{-i\mathbf{q}\cdot\mathbf{r}}\psi_{\mathbf{k}+\mathbf{q}a'}(\mathbf{r})d\mathbf{r} \right|^2, \tag{8}$$

with $f_{\mathbf{k},a} = 1(0)$ for occupied (unoccupied) bands.

We approximate the quasiparticle eigenfunction by the TB model

$$\psi_{\mathbf{k},a} = \frac{1}{\sqrt{N_u}} \sum_{s=A,B} \sum_{u=1}^{N_u} C_s^a(\mathbf{k})e^{i\mathbf{k}\cdot\mathbf{R}_{us}}\phi(\mathbf{r} - \mathbf{R}_{us}), \tag{9}$$

with N_u the number of graphene unit cells in the SWNT, $C_s^a(s = A, B)$ the wave function coefficient, and ϕ the atomic wave function.

Substituting Eq. (9) into Eq. (3), we find that there is a four center integral in the Coulomb interaction,

$$I = \int d\mathbf{r}' d\mathbf{r} \phi(\mathbf{r}' - \mathbf{R}_{t1'})\phi(\mathbf{r}' - \mathbf{R}_{t2'})$$
$$\times v(|\mathbf{r} - \mathbf{r}'|)\phi(\mathbf{r} - \mathbf{R}_{t1})\phi(\mathbf{r} - \mathbf{R}_{t2}). \tag{10}$$

Here, we define $t = (u, s)$ for convenience. The largest contribution to this integral is the case with $t1' = t2' = t'$ and $t1 = t2 = t$. By adopting this approximation, the Coulomb interaction is given by

$$V(\mathbf{k}_1a_1\mathbf{k}_2a_2, \mathbf{k}_3a_3\mathbf{k}_4a_4)$$
$$= \delta(\mathbf{k}_2 - \mathbf{k}_1, \mathbf{k}_4 - \mathbf{k}_3) \sum_{s',s} C_{s'}^{a_1*}(\mathbf{k}_1)C_{s'}^{a_2}(\mathbf{k}_2)$$
$$\times C_s^{a_3}(\mathbf{k}_3)C_s^{a_4*}(\mathbf{k}_4)v_{s',s}(\mathbf{k}_2 - \mathbf{k}_1), \tag{11}$$

with $v_{s',s}(\mathbf{q})$ the Fourier transformation (FT) of the Coulomb potential

$$v_{s',s}(\mathbf{q}) = \frac{1}{N_u} \sum_{u'} e^{i\mathbf{q}\cdot(\mathbf{R}_{u's'}-\mathbf{R}_s)} \int d\mathbf{r}' d\mathbf{r}\, v(|\mathbf{r}-\mathbf{r}'|)$$
$$\times |\phi(\mathbf{r}'-\mathbf{R}_{u's'})|^2 |\phi(\mathbf{r}-\mathbf{R}_s)|^2. \quad (12)$$

The FT of the Coulomb potential can further be approximated by

$$v_{s',s}(\mathbf{q}) = \frac{1}{N_u} \sum_{u'} e^{i\mathbf{q}\cdot(\mathbf{R}_{u's'}-\mathbf{R}_{0s})} v(|\mathbf{R}_{u's'}-\mathbf{R}_{0s}|). \quad (13)$$

The unscreened Coulomb potential $v(\mathbf{r})$ between carbon π orbitals is modeled by the Ohno potential[23]

$$v(|\mathbf{R}_{u's'}-\mathbf{R}_{0s}|) = \frac{U}{\sqrt{\left(\frac{4\pi\epsilon_0}{e^2} U|\mathbf{R}_{us}-\mathbf{R}_{0s'}|\right)^2 + 1}}, \quad (14)$$

where U is the energy cost to place two electrons on a single site $(|\mathbf{R}_{us}-\mathbf{R}_{s'}|=0)$ and U is taken as $U \equiv U_{\pi_a \pi_a \pi_a \pi_a} = 11.3$ eV for π orbitals.[23]

The direct and exchange terms in Eq. (3) can now be expressed by the wave function coefficients

$$K^d(\mathbf{k}_c'\mathbf{k}_v',\mathbf{k}_c\mathbf{k}_v) = \delta(\mathbf{k}_c'-\mathbf{k}_v',\mathbf{k}_c-\mathbf{k}_v) \sum_{s',s} C_{s'}^{c^*}(\mathbf{k}_c') C_{s'}^c(\mathbf{k}_c)$$
$$\times C_s^v(\mathbf{k}_v') C_s^{v^*}(\mathbf{k}_v) v_{s',s}(\mathbf{k}_c'-\mathbf{k}_c)/\epsilon(\mathbf{k}_c'-\mathbf{k}_c),$$

$$K^x(\mathbf{k}_c'\mathbf{k}_v',\mathbf{k}_c\mathbf{k}_v) = \delta(\mathbf{k}_c'-\mathbf{k}_v',\mathbf{k}_c-\mathbf{k}_v) \sum_{s',s} C_{s'}^{c^*}(\mathbf{k}_c') C_{s'}^v(\mathbf{k}_v')$$
$$\times C_s^c(\mathbf{k}_c) C_s^{v^*}(\mathbf{k}_v) v_{s',s}(\mathbf{k}_c'-\mathbf{k}_v')/\epsilon(\mathbf{k}_c'-\mathbf{k}_v'). \quad (15)$$

With the help of Eq. (9), the integral in the polarization $\Pi(\mathbf{q})$ of Eq. (8) is expressed as

$$\int \psi_{\mathbf{k}a}^*(\mathbf{r}) e^{-i\mathbf{q}\cdot\mathbf{r}} \psi_{\mathbf{k}+\mathbf{q}a'}(\mathbf{r}) d\mathbf{r}$$
$$= \sum_{u's's} C_{s'}^{a^*}(\mathbf{k}) C_s^{a'}(\mathbf{k}+\mathbf{q}) e^{i[-\mathbf{k}\cdot\mathbf{R}_{u's'}+(\mathbf{k}+\mathbf{q})\cdot\mathbf{R}_{0s}]}$$
$$\times \int d\mathbf{r}\, \phi^*(\mathbf{r}-\mathbf{R}_{u's'}) e^{-i\mathbf{q}\cdot\mathbf{r}} \phi(\mathbf{r}-\mathbf{R}_{0s})$$
$$\approx \sum_s C_s^{a^*}(\mathbf{k}) C_s^{a'}(\mathbf{k}+\mathbf{q}). \quad (16)$$

Using Eq. (16), the polarization $\Pi(\mathbf{q})$ can be expressed by the wave function coefficient
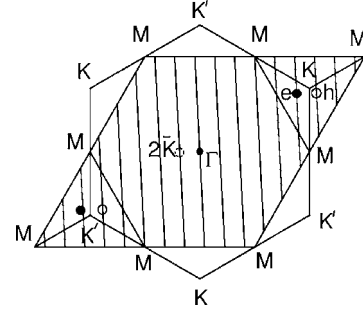

FIG. 1. The three inequivalent regions in the 2D BZ of graphene. The cutting lines for a (6,5) SWNT are shown. The electron-hole pairs and the corresponding center-of-mass momentum $2\bar{\mathbf{K}}=\mathbf{k}_c-\mathbf{k}_v$ for an $E_{12}(E_1)$ exciton of the (6,5) SWNT are indicated. The electron-hole pair with the electron and hole lying on the second and first cutting lines to the K point and the electron-hole pair with the electron and hole lying on the first and second cutting lines to the K' point correspond to an $E_{12}(E_1)$ exciton with the center-of-mass momentum $2\bar{\mathbf{K}}$ on the first cutting line to the Γ point.

$$\Pi(\mathbf{q}) = -2 \sum_{\mathbf{k}} \left[\frac{\left| \sum_s C_s^{v^*}(\mathbf{k}) C_s^c(\mathbf{k}+\mathbf{q}) \right|^2}{\epsilon_{\mathbf{k}+\mathbf{q}v} - \epsilon_{\mathbf{k}v}} + \frac{\left| \sum_s C_s^{c^*}(\mathbf{k}) C_s^v(\mathbf{k}+\mathbf{q}) \right|^2}{\epsilon_{\mathbf{k}c} - \epsilon_{\mathbf{k}+\mathbf{q}v}} \right]. \quad (17)$$

In the dielectric function expression of Eq. (7),

$$v(\mathbf{q}) = \frac{1}{4} \sum_{s',s} v_{s',s}(\mathbf{q}). \quad (18)$$

Consider a single electron-hole pair excitation in which an electron in a state of wave number $\mathbf{k}_v$ in the valence band is promoted to a state of wave number $\mathbf{k}_c$ in the conduction band. We can introduce new variables $\mathbf{k}$ and $\bar{\mathbf{K}}$ so that

$$\mathbf{k}_c = \mathbf{k} + \bar{\mathbf{K}} \quad \text{and} \quad \mathbf{k}_v = \mathbf{k} - \bar{\mathbf{K}}, \quad (19)$$

and denote the excited state as $|\mathbf{k}, \bar{\mathbf{K}}\rangle$. Here $\mathbf{k}$ and $2\bar{\mathbf{K}}$ are the wave numbers of the relative motion and the center-of-mass motion, respectively, of the electron-hole pair.

The BS equation in this representation is written as

$$\{[E(\mathbf{k}+\bar{\mathbf{K}},c) - E(\mathbf{k}-\bar{\mathbf{K}},v)] + K(\mathbf{k}'\bar{\mathbf{K}},\mathbf{k}\bar{\mathbf{K}})\}\Psi^n(\mathbf{k}\bar{\mathbf{K}})$$
$$= \Omega_n \Psi^n(\mathbf{k}'\bar{\mathbf{K}}). \quad (20)$$

Equation (20) indicates that the center-of-mass motion $\bar{\mathbf{K}}$ is a good quantum number.

As shown in Fig. 1, there are three inequivalent regions in the two-dimensional (2D) Brillouin zone (BZ) of graphene, i.e., two triangle regions around K, K' and one hexagonal region around the Γ point. In the case of SWNTs, the allowed wave vectors are on the so called cutting lines[33,34] and can be expressed by $\mathbf{k} = \mu \mathbf{K}_1 + k\mathbf{K}_2/|\mathbf{K}_2|.$[1] Here $\mathbf{K}_1$ and $\mathbf{K}_2$ are, respectively, the reciprocal lattice vectors along the cir-

TABLE I. Ohno parameter $U_{o_1'o_2',o_1o_2}/U_{\pi_a\pi_a\pi_a\pi_a}$ values [Eq. (24)].

$ssss$	$ss\sigma\sigma$	$ss\pi\pi$	$\sigma\sigma\sigma\sigma$	$\sigma\sigma\pi\pi$	$\pi_a\pi_a\pi_a\pi_a$	$\pi_a\pi_a\pi_b\pi_b$
0.90	0.91	0.91	1.00	0.89	1.00	0.89
$sss\sigma$	$s\sigma s\sigma$	$s\sigma\sigma\sigma$	$s\sigma\pi\pi$	$s\pi\sigma\pi$	$\pi_a\pi_b\pi_a\pi_b$	$\sigma\pi\sigma\pi$
1.15×10^{-3}	0.19	5.47×10^{-4}	4.12×10^{-4}	8.46×10^{-4}	5.30×10^{-2}	0.269

cumferential and axial directions.[1] In this paper, the cutting line index (integer μ) and the 1D wave vectors (k) are confined to lie within the parallelogram in Fig. 1, which shows that the cutting lines of a SWNT are also distributed in the three inequivalent regions.

The excitons in SWNTs can then be classified according to the $2\bar{K}$ in these three different regions. The optical transitions will be related to the electron and hole in the K or K' regions. If both the electron ($\mathbf{k}_c$) and hole ($\mathbf{k}_v$) are from the K (or K') region, then $2\bar{K}=\mathbf{k}_c-\mathbf{k}_v$ lies in the Γ region and the corresponding exciton is an A exciton. If an electron is from the K region and a hole is from the K' region, $2\bar{K}$ lies in the K region and this exciton is an E exciton. If an electron is from the K region and a hole is from the K' region, $2\bar{K}$ lies in the K' region and this exciton is an E^* exciton. In this paper, for simplicity we sometimes call the excitons with $2\bar{K}$ in Γ region A excitons. According to linear group theory, A excitons can be further classified into A and E_μ symmetry excitons. If $2\bar{K}$ lies on a cutting line passing through Γ point, the exciton is an A symmetry exciton; otherwire it is an E_μ symmetry exciton with μ the cutting line index for $2\bar{K}$

For A excitons, the electron-hole pair $|\mathbf{k}_c,\mathbf{k}_v\rangle=|\mathbf{k},\bar{K}\rangle$ with the electron and hole from the K region, and $|-\mathbf{k}_v,-\mathbf{k}_c\rangle$ $=|-\mathbf{k},\bar{K}\rangle$ with the electron and hole from the K' region have the same $\bar{K}$. Thus, we can recombine these two electron-hole pairs to get

$$A_{2,1}=|\mathbf{k},\pm,\bar{K}\rangle=\frac{1}{\sqrt{2}}(|\mathbf{k},\bar{K}\rangle\pm|-\mathbf{k},\bar{K}\rangle). \qquad (21)$$

Here $|\mathbf{k},+,\mathbf{K}\rangle$ and $|\mathbf{k},-,\mathbf{K}\rangle$ are antisymmetric and symmetric, respectively, under the C_2 rotation around the axis perpendicular to the nanotube axis. The corresponding excitons are antisymmetric and symmetric under the C_2 rotation and are labeled as A_2 and A_1 excitons, respectively. The classification of excitons in SWNTs here is consistent with that by group theory within the group of the wave vector approach. This is exact for the most general chiral SWNTs, while for achiral SWNTs more symmetries should be considered.[35] After symmetry considerations, the quasiparticle energy and kernel for A excitons can be expressed as

$$E(\mathbf{k}+\bar{K},A_{2,1})=[E(\mathbf{k}+\bar{K})+E(-\mathbf{k}+\bar{K})]/2,$$

$$K(\mathbf{k}',\mathbf{k};\pm,\bar{K})=[K(\mathbf{k}',\mathbf{k};\bar{K})+K(-\mathbf{k}',-\mathbf{k};\bar{K})]/2,$$

$$\pm[K(\mathbf{k}',-\mathbf{k};\bar{K})+K(-\mathbf{k}',\mathbf{k};\bar{K})]/2=K(\mathbf{k}',\mathbf{k};\bar{K})\pm K(\mathbf{k}',$$

$$-\mathbf{k};\bar{K}), \qquad (22)$$

where K is either K^d or K^x. In the derivation of Eq. (22), we have used the relationship $K(\mathbf{k}',\mathbf{k};\bar{K})=K(-\mathbf{k}',-\mathbf{k};\bar{K})$. For the exchange term K^x, we further have a relationship $K^x(\mathbf{k}',\mathbf{k};\bar{K})=K^x(\mathbf{k}',-\mathbf{k};\bar{K})$ and thus we have

$$K^x(\mathbf{k}',\mathbf{k};+,\bar{K})=2K^x(\mathbf{k}',\mathbf{k};\bar{K}),$$

$$K^x(\mathbf{k}',\mathbf{k};-,\bar{K})=0. \qquad (23)$$

Equation (23) indicates that for A_1 excitons the spin singlet and triplet states are degenerate.

In the extended TB (ETB) model, we consider atomic s, p_x, p_y, and p_z orbitals that form the σ and π molecular orbitals. Thus, the quasiparticle wave function coefficient C_s^a in Eq. (9) should be replaced by $C_{s,o}^a$ with $o=s$, σ, and π. Here the unscreened Coulomb potential between all orbitals is approximated by the Ohno potential. The parameter $U_{o_1'o_2',o_1o_2}$ for $o,o'=s,\sigma,\pi$, in the Ohno potential [U in Eq. (14)] is defined as

$$U_{o_1'o_2',o_1o_2}=\int d\mathbf{r}d\mathbf{r}'\,\phi_{o_1'}^*(\mathbf{r})\phi_{o_2'}(\mathbf{r})\frac{e^2}{|\mathbf{r}-\mathbf{r}'|}\times\phi_{o_1}^*(\mathbf{r}')\phi_{o_2}(\mathbf{r}'). \qquad (24)$$

Due to the orbital symmetry, only a few of the 256 $U_{o_1'o_2',o_1o_2}$ parameters have nonzero values.[36] We calculate these 14 nonzero U parameters by using the atomic wave functions and the Kohn-Sham potential from Porezag *et al.*[37] and the ratios $U_{o_1'o_2',o_1o_2}/U_{\pi_a\pi_a,\pi_a\pi_a}$ are listed in Table I. The p orbitals from two carbon atoms can form σ, π_a and π_b orbitals with σ and π_b orbitals, respectively, along the bond connecting the two carbon and tube axis directions and π_a is perpendicular to both the σ and π_b orbitals. In Table I, π is used to denote either the π_a or π_b orbital. From Table I, it is seen that U values for $(sss\sigma)$, $(s\sigma\sigma\sigma)$, $(s\sigma\pi\pi)$, and $(s\pi\sigma\pi)$ are quite small compared to the $(\pi_a\pi_a\pi_a\pi_a)$ case and can be neglected. For the remaining cases with non-negligible U values, except for the $(\pi_a\pi_a\pi_a\pi_a)$ case, the Coulomb interaction is associated with at least two orbitals other than the π_a orbital. For π band electronic states, the wave function coefficient $C_{s,o}^a$ for an orbital other than the π_a orbital is generally one order of magnitude smaller than that for the π_a orbital. From Eq. (15), it follows that the Coulomb interaction for a case other than the $(\pi_a\pi_a\pi_a\pi_a)$ case is at least two orders smaller than that for the $(\pi_a\pi_a\pi_a\pi_a)$ case. Thus, the effect from the modification of the electronic structure by
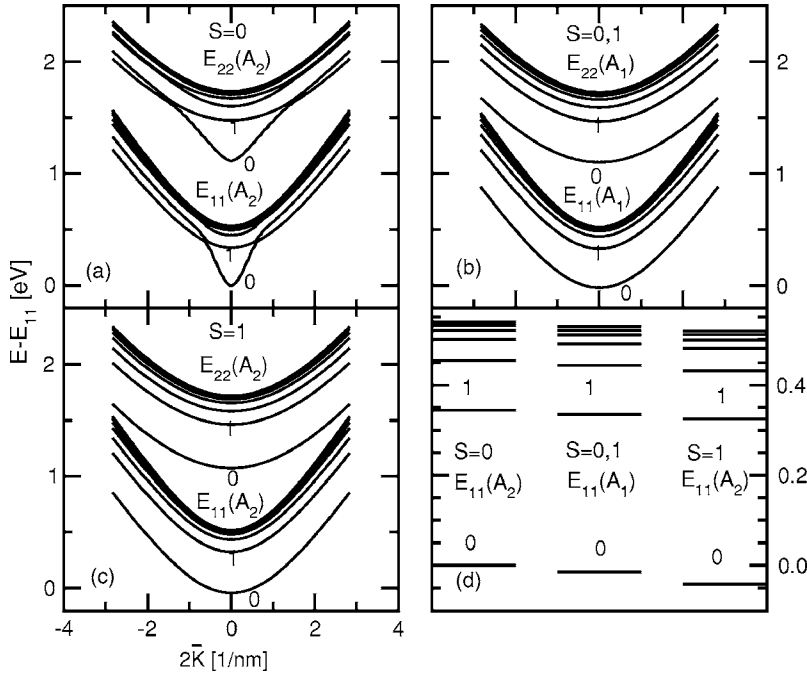
FIG. 2. The excitation energy dispersions for (a) $E_{11}(A_2)$ ($S=0$) and $E_{22}(A_2)$ ($S=0$), (b) $E_{11}(A_1)$ ($S=0,1$) and $E_{22}(A_1)$ ($S=0,1$), and (c) $E_{11}(A_2)$ ($S=1$) and $E_{22}(A_2)$ ($S=1$) excitons for (6,5) SWNTs. The excitation energy levels for $\bar{K}=0$ excitons are also shown in (d).

σ-π rehybridization will only bring a weak contribution to the Coulomb interaction and therefore simple TB can approximately describe the Coulomb interaction. However, as we know, the ETB model is essential to explain the larger family spread in the Kataura plot.[2] Moreover, structure optimization brings additional modifications in the family patterns. Therefore, in this paper we will first study a general picture of exciton effects by using the simple TB model, and the exciton Kataura plot will then be calculated by using the ETB, from which the origin of the large family spread will be discussed. For the simple TB model, we use the nearest neighbor TB parameter $\gamma_0=2.7$ eV.[28] For the ETB model, we use the same TB parameters as those used in the free-particle ETB,[2,3] which are calculated by density functional theory.[37]

III. EXCITON WAVE FUNCTIONS

Since the photon wave vector is nearly zero, the E and E^* excitons, which possess a large angular momentum for the center-of-mass momentum, are dark excitons. It is known that the optical dipole moment is defined as $M \propto \mathbf{P} \cdot \langle \Psi | \nabla | \Psi_0 \rangle$ with $\langle \Psi |$ and $| \Psi_0 \rangle$ denoting the excited and ground states, respectively, and $\mathbf{P}$ denoting the light polarization vector. The ground state $| \Psi_0 \rangle$ has an s symmetry and ∇ is antisymmetric under the C_2 rotation. Thus, to have a nonzero M, $| \Psi \rangle$ should also be antisymmetric under the C_2 rotation. Therefore, A_1 excitons are also dark excitons and only A_2 excitons are bright excitons.[35] A simple and clear way to label exciton states is to consider both the previous notation E_{ij} used for the optical level and the exciton symmetries. For example, $E_{ij}(A)$ means that the electron and hole for an A exciton lie, respectively, on the ith and jth cutting lines with respect to the K point of the 2D BZ of graphene. Due to angular momentum conservation, $E_{ii}(A_2)$, where an electron and a hole lie on the same cutting line, and $E_{ii+1}(E_1)$ [or

$E_{i+1i}(E_1)$], where an electron and a hole lie on two nearest-neighbor cutting lines, are optically active excitons for light polarized parallel and perpendicular to the nanotube axis, respectively. Although dark excitons are not optically active, they play an important role in Raman spectroscopy. For example, from momentum conservation, we know that the Raman G' and D bands could be associated with the exciton scattering processes by phonons between bright A exciton states and dark E or E^* states.

We calculated excitation energy dispersions as a function of the center-of-mass momentum $2\bar{K}$. Figures 2(a)–2(c) show the results for $E_{ii}(A)$ excitons for a (6, 5) SWNT. It is seen that exciton states are assembled according to their cutting lines.[33,34] Within the same cutting line, the discrete exciton states gradually turn to be unbound electron-hole continuum bands with increasing excitation energy. We use the index $\nu=0,1,2\ldots$ to label $\bar{K}=0$ excitons as $E_{ii}(A^\nu)$ to indicate the order of magnitude of the excitation energy. Figure 2(d) gives the excitation energy levels for $\bar{K}=0$ $E_{11}(A^\nu)$ states. We note that for spin $S=1$ states, $E_{11}(A_2^0)$ has a bit larger energy than $E_{11}(A_1^0)$. From Eq. (22), it is known that for the states with the same spin, the energy difference between $E_{11}(A_2)$ and $E_{11}(A_1)$ is determined by the Coulomb energy $K(\mathbf{k'}, -\mathbf{k}; \pm, \bar{K})$, which is the energy for an intervalley scattering process and thus has a one order of magnitude smaller energy than the energy for an intravalley scattering process, $K(\mathbf{k'}, \mathbf{k}; \pm, \bar{K})$. Therefore, the energy difference between $E_{11}(A_2^0)$ ($S=0$) and $E_{11}(A_1^0)$ is quite small [about 12 meV in Fig. 2(d)]. Moreover, in Fig. 2(d) the triplet $E_{11}(A_2^0)$ state has about a 35 meV smaller energy than the singlet $E_{11}(A_2^0)$ state. The energy difference between the triplet and singlet $E_{11}(A_2)$ states is determined by the exchange Coulomb interaction $K^x(\mathbf{k'}, \mathbf{k}; \bar{K})$ [see Eq. (23)], which is about one order of magnitude smaller than the direct Coulomb interaction

$K^d(\mathbf{k}',\mathbf{k};\bar{\mathbf{K}})$ in SWNTs. The energy difference between the singlet $E_{11}(A_2^0)$ state and $E_{11}(A_1^0)$ state and that between the singlet and triplet $E_{11}(A_2^0)$ states are consistent with those found by previous calculations.[22,24] Hereafter, we will mainly discuss the singlet bright exciton $E_{ij}(A_2^0)$ state with $\bar{K}=0$.

The exciton wave function for an A_2 exciton with an electron and hole on $(u's')$ and (us) sites can be expressed as

$$\Psi_{\bar{\mathbf{K}}}^n(u's',us) = 2e^{i\bar{\mathbf{K}}\cdot(\mathbf{R}_{u's'}+\mathbf{R}_{us})}\sum_{\mathbf{k}}\Psi_{\bar{\mathbf{K}}}^n(\mathbf{k})\mathrm{Re}[C_{s'}^c(\mathbf{k}+\bar{\mathbf{K}})$$

$$\times C_s^{v*}(\mathbf{k}-\bar{\mathbf{K}})e^{i\mathbf{k}\cdot(\mathbf{R}_{u's'}-\mathbf{R}_{us})}]. \qquad (25)$$

Here $\Psi_{\bar{\mathbf{K}}}^n(\mathbf{k})$ is the exciton wave function in reciprocal space, which is obtained by solving the BS equation of Eq. (20). For an $E_{ii}(A_2)$ exciton with $\bar{\mathbf{K}}=0$, Eq. (25) becomes

$$\Psi_0^n(u's',us) = \sum_{\mathbf{k}}\Psi_0^n(\mathbf{k})\mathrm{Re}[C_{s'}^c(\mathbf{k})C_s^{*v}(\mathbf{k})e^{i\mathbf{k}\cdot(\mathbf{R}_{u's'}-\mathbf{R}_{us})}].$$

$$(26)$$

For an $E_{ii+1}(E_1)$ exciton, $\bar{\mathbf{K}}=(1,0)=\bar{\mathbf{K}}_1$, and Eq. (25) turns to be

$$\Psi_+^n(u's',us) = 2e^{i(\theta_{u's'}+\theta_{us})}\sum_{\mathbf{k}}\Psi_{(1,0)}^n(\mathbf{k})\mathrm{Re}[C_{s'}^c(\mathbf{k}+\bar{\mathbf{K}})$$

$$\times C_s^{v*}(\mathbf{k}-\bar{\mathbf{K}})e^{i\mathbf{k}\cdot(\mathbf{R}_{u's'}-\mathbf{R}_{us})}]. \qquad (27)$$

For an $E_{i+1i}(E_1)$ exciton, $\bar{\mathbf{K}}=-\bar{\mathbf{K}}_1$ and thus we have the following relation for the wave function $\Psi_-^n(u's',us) = \Psi_+^{n*}(u's',us)$. The center-of-mass momentum is opposite for $E_{i+1i}(E_1)$ and $E_{ii+1}(E_1)$ excitons, and thus $E_{i+1i}(E_1)$ and $E_{ii+1}(E_1)$ are degenerate states. Therefore, we can take $\Psi_{+1}^n(u's',us)=\mathrm{Re}[\Psi_+^n(u's',us)]$, and $\Psi_{-1}^n(u's',us) = \mathrm{Im}[\Psi_+^n(u's',us)]$ as two real wave functions for the $E_{ii+1}(E_1)$ and $E_{i+1i}(E_1)$ states.

In Fig. 3 we show the wave functions along a line passing through an A carbon site parallel to the nanotube axis of an $(8,0)$ SWNT for several $E_{22}(A_2^\nu)$ excitons with lower excitation energies with $\nu=0$, 1, and 2. We put the hole at an A site. The wave functions with a hole at a B site are similar. For the $E_{22}(A_2^0)$ and $E_{22}(A_2^2)$ states, the electron can be either at A or B sites, i.e., (A,A), (A,B), (B,A), and (B,B) are allowed, and the wave functions are similar to each other. In Fig. 3, we show these results for the (A,A) case. However, for the $E_{22}(A_2^1)$ state, the electron and hole can not be on the same type of atom site, i.e., (A,A) or (B,B) is not allowed. Thus, the wave function for this state in Fig. 3 is for the (A,B) case. It is seen from Fig. 3 that the $E_{22}(A_2^0)$ and $E_{22}(A_2^2)$ excitons are symmetric and the $E_{22}(A_2^1)$ exciton is antisymmetric under z reflection. It follows that $E_{22}(A_2^0)$ and $E_{22}(A_2^2)$ excitons are bright and the $E_{22}(A_2^1)$ exciton is dark with respect to parallel polarized linear light. In the two-photon experiments, the $E_{22}(A_2^2)$ exciton becomes bright.[13] For an achiral (armchair or zigzag) SWNT, exciton wave functions are either even or odd functions of z because of the inversion center in the SWNT. Thus, we use A_{2u} or A_{2g} to label an A_2
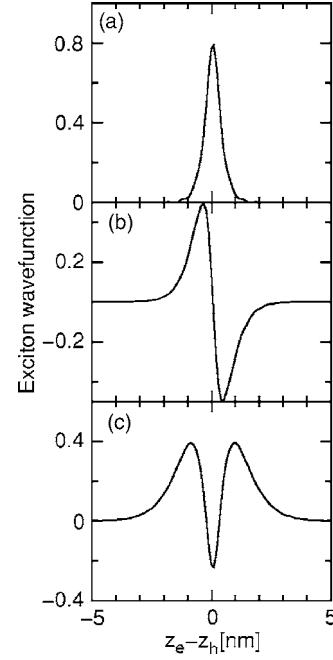

FIG. 3. The exciton wave functions along a line passing through an A carbon site parallel to the tube axis of an $(8,0)$ SWNT. (a) $E_{22}(A_2^0)$, (b) $E_{22}(A_2^1)$, and (c) $E_{22}(A_2^2)$ are the exciton wavefunctions for the three lowest $E_{22}(A_2^\nu)$ excitations in the order of increasing energy. The hole is put on an A atom.

exciton in an achiral SWNT, which is symmetric or antisymmetric under σ_h reflection $(z\to-z)$, respectively.[35] In Fig. 3, $E_{22}(A_2^0)$ and $E_{22}(A_2^2)$ states are A_{2g} states and the $E_{22}(A_2^1)$ state is an A_{2u} state. From the $E_{22}(A_2^0)$ to the $E_{22}(A_2^2)$ state, the excitation energy increases and the wave function's delocalized length increases. The half-width of the wave function (l) in real space for the $E_{22}(A_2^0)$ state is about 1 nm for an $(8,0)$ SWNT.

To study the wave function size dependence on chirality systematically, we calculate the wave functions for the $E_{11}(A_2^0)$ and $E_{22}(A_2^0)$ states for all SWNTs with diameters (d_t) in the range of 0.5 nm $<d_t<1.6$ nm. The wave function half-width (l_k) in the 1D k space, k width at a half maximum of $\Psi(\mathbf{k})$, is shown in Fig. 4. For comparison, the cutting line spacing $2/d_t$ is also shown by the solid line. It is interesting to see in Fig. 4 that l_k is always smaller than the cutting line spacing $2/d_t$. Further, the $E_{ii}(A_2^0)$ state has a larger l_k than the $E_{ii}(A_2^\nu)$ states with $\nu=1,2,\dots$. Since l_k measures the extended length of a wave function in k space, this result indicates that one cutting line is sufficient to describe $E_{ii}(A)$ states. Generally, we can say that the ith cutting line is sufficient to describe $E_{ii}(A)$, $E_{ii}(E)$, and $E_{ii}(E^*)$ states, and that the ith and $(i+1)$-th cutting lines are sufficient to describe $E_{ii+1}(E_1)$ and $E_{i+1i}(E_1)$ states. Since metallic (M) SWNTs have a smaller binding energy and thus smaller l_k than semiconducting (S) SWNTs, the above conclusion is also valid for M SWNTs. Due to the fact that one cutting line is sufficient to describe E_{ii} states, the matrix dimension for the BS equation in Eq. (20) can be dramatically decreased.

Figure 4 shows that l_k decreases with d_t and $E_{22}(A_2^0)$ has a larger l_k than $E_{11}(A_2^0)$, which is consistent with the fact
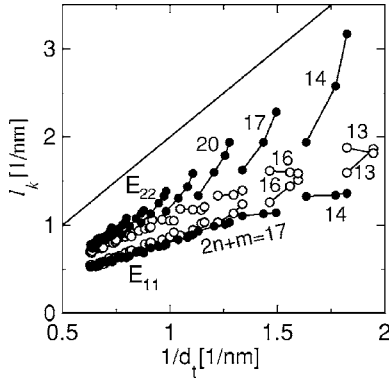
FIG. 4. The half width l_k of the wave functions in 1D k space for $E_{11}(A_2^0)$ and $E_{22}(A_2^0)$ states for many SWNTs. The cutting line spacing $2/d_t$ is shown by the solid line for comparison. Open and filled circles are for SI and SII SWNTs. Integers denote $2n+m$ family values.

FIG. 6. The wave function Ψ_{-1} for $E_{12}(E_1^0)$ or $E_{21}(E_1^0)$ along a line on the circumference of an (8,0) SWNT. The hole indicated by a small circle is put at an A atom with $\theta \approx -11°$. (a) Ψ_{-1} on the unfolded line and (b) $|\Psi_{-1}|$ on the folded line.

shown below, that the exciton binding energy decreases with increasing d_t and $E_{22}(A_2^0)$ has a larger binding energy than $E_{11}(A_2^0)$. Also, l_k shows a tube type (SI or SII) dependence and $(2n+m)$-family patterns. For E_{11} states, SI SWNTs have a larger l_k than SII SWNTs. Within the same $(2n+m)$-family (similar d_t), l_k for SI SWNTs decreases with increasing chiral angle, while l_K for SII SWNTs increases with θ. For E_{22} states, in contrast, SII SWNTs have a larger l_k than SI SWNTs. Within the same $(2n+m)$-family, l_k for SII SWNTs decreases with θ while l_k for SI SWNTs increases with θ.

Although the exciton wave function along the tube axis is localized, it is known that the wave function along the circumference is extended. Actually, Fig. 4 already shows that l_k is smaller than the cutting line spacing in k space, indicating that in real space l is larger than d_t. The wave function Ψ_0 along a line on the circumference of an (8,0) SWNT is shown in Fig. 5 for the $E_{22}(A_2^0)$ state. It is seen that the electron is homogeneously distributed in the circumferential direction when the hole position is fixed, indicating that there is no dipole in the circumferential direction. The oscillation of the function in Fig. 5 comes from the phase factor $e^{i\mu(\theta_e-\theta_h)}$ in Eq. (26) with $\mu=6$ for the second cutting line,

and θ_e (θ_h) is the angle for the electron (hole) position on the circumference.

Figures 6 and 7 show the wave function Ψ_{-1} along a line on the circumference of an (8,0) SWNT for $E_{12}(E_1^0)$ or $E_{21}(E_1^0)$ states, respectively. As we have mentioned Ψ_{-1} is the imaginary part of Ψ_+ in Eq. (27). All A (or B) atoms in an (8,0) SWNT are distributed on the circumference with an angle spacing $\Delta\theta=45°$. As an example, Fig. 6 shows Ψ_{-1} by putting the hole at an A atom with $\theta_h \approx -11°$. Figure 6 shows that the electron prefers to be distributed on the opposite side to the hole, and therefore a dipole moment perpendicular to the nanotube axis appears. The formation of the dipole is due to the phase factor $e^{i(\theta_e+\theta_h)}$ in Eq. (27). Similar to an $E_{ii}(A_2)$ state, the phase factor $e^{i\mu_i(\theta_e-\theta_h)}$ in Eq. (27) will also bring in an oscillation with a period of $2\pi/\mu_i$ to an $E_{ii+1}(E_1)$ or $E_{i+1i}(E_1)$ state. However, unlike an $E_{ii}(A_2)$ state, there is another phase factor $e^{i(\theta_e+\theta_h)}$ in Eq. (27). This phase factor comes from the fact that the electron and hole in an $E_{ii+1}(E_1)$ $[E_{i+1i}(E_1)]$ state are from two cutting lines with $\mu_{i+1}-\mu_i=1$. The phase factor $e^{i(\theta_e+\theta_h)}$ will then adjust the amplitude of the oscillation from $e^{i\mu_i(\theta_e-\theta_h)}$ by a $\cos(\theta_e+\theta_h)$ or $\sin(\theta_e+\theta_h)$ function. This adjustment will bring in a dipole, perpendicu-
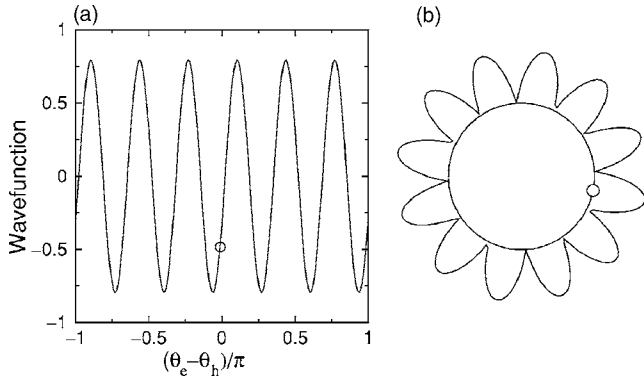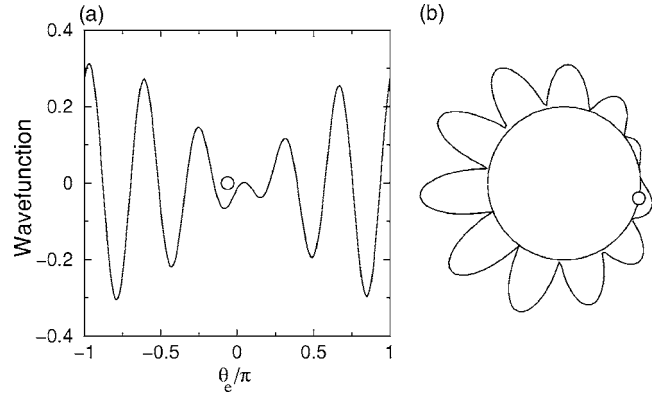

FIG. 5. The wave function Ψ_0 of the $E_{22}(A_2^0)$ state along a line on the circumference of an (8,0) SWNT. (a) Ψ_0 on the unfolded line and (b) $|\Psi_0|$ on the folded line. The small open circles in (a) and (b) denote the hole position.
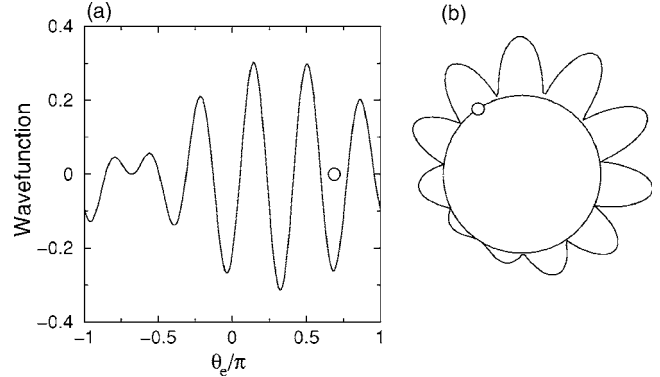

FIG. 7. The wave function Ψ_{-1} for $E_{12}(E_1^0)$ or $E_{21}(E_1^0)$ along a line on the circumference of an (8,0) SWNT. The hole indicated by a small circle is put at an A atom with $\theta \approx 126°$. (a) Ψ_{-1} on the unfolded line and (b) $|\Psi_{-1}|$ on the folded line.

lar to the tube sidewall. Interestingly, $e^{i(\theta_e+\theta_h)}$ indicates that the electron distribution will depend on the hole position θ_h. As an example, in Fig. 7 we show the wave function Ψ_{-1} with the hole at an A atom with $\theta_h \approx 126°$. Although the electron also prefers to occupy the sites opposite to the hole site in Fig. 7, the position with the largest possibility for finding an electron is closer to the hole compared to that in Fig. 6. We call this dipole a "circumference dipole" and we call the dipole formed along the nanotube axis direction by a bound electron-hole pair an "axis dipole." The formation of the "circumference dipole" is important for explaining the experimental observations using perpendicularly polarized light, which shows that $E_{12}(E_1)$ excitation energies are very close to the $E_{22}(A_2^0)$ excitation energy, and it should be pointed out that this observation can not be explained by a single-particle picture.[38] Uryu and Ando have pointed out that the depolarization effect will reduce the circumference dipole moment and thus reduce the Coulomb interaction between the electron and hole, leading to a smaller exciton binding energy for $E_{12}(E_1)$ states as compared to $E_{11}(A_2^0)$ and $E_{22}(A_2^0)$ states, and this fact is essential to get the enhanced $E_{12}(E_1)$ excitation energy that is needed to explain the experimental observations.[38,39]

In the present work, the dielectric screening is treated within the RPA. For the cases shown in Figs. 6 and 7, where an electron and a hole are located on the opposite sides of the diameter of a SWNT, the screening effect is reduced compared with Eq. (7). By considering that both the exciton binding energies and the self-energies depend critically on the screening function, a dielectric function calculation beyond the RPA is needed for these cases. The calculation of the excitation and binding energies for the perpendicular polarization case is beyond the scope of this paper.

IV. FAMILY PATTERNS IN EXCITATION AND BINDING ENERGIES

A. Exciton binding energy

We calculate the excitation and binding energies for all SWNTs with d_t in the range of 0.5 nm $< d_t <$ 1.6 nm for $E_{ii}(A_2^0)$ states for S and M SWNTs. The resulting excitation energy E_{ii} and exciton binding energy E_{bd} Kataura plots are shown in Fig. 8. From Fig. 8(a) we see that the chiral angle dependence of E_{ii} is quite weak. Thus, the results based on the simple TB model are not sufficient to explain the large family spread in the excitation Kataura plot observed by experiments.[2] From the following discussion we will see that this excitation energy family spread problem can be solved by the ETB.[2] From Fig. 8, it is clear that the exciton binding energy shows both a diameter and chiral angle dependence. In Fig. 8(b), E_{22} states for S SWNTs (E_{22}^S) have a larger binding energy than E_{11}^S states, which is consistent with the results calculated by Ando.[28] Moreover, the exciton binding energy shows a clear type I and II dependence and also $(2n+m)$-family patterns. The type dependence and family patterns in the binding energy are similar to those in the wave function size in k space (see Fig. 4). The chiral angle dependence of E_{bd} is understood by the chiral angle depen-
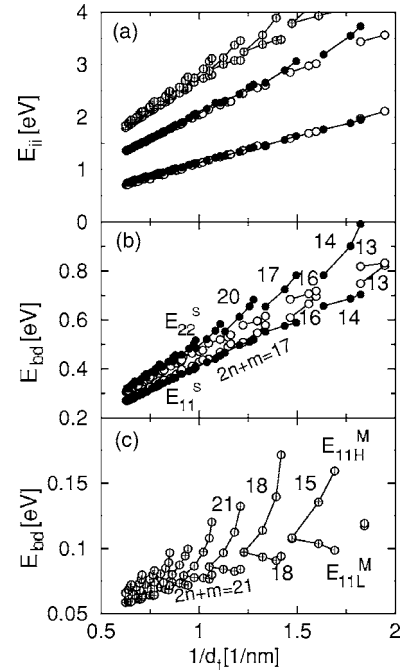

FIG. 8. The excitation and binding energy Kataura plots using the simple TB model for $E_{11}^S(A_2^0)$ and $E_{22}^S(A_2^0)$ states in S SWNTs and $E_{11L}^M(A_2^0)$ and $E_{11H}^M(A_2^0)$ states in M SWNTs. (a) Excitation energy Kataura plot. Open, filled, and crossed circles are for SI, SII, and M SWNTs. (b) Binding energy Kataura plots for S SWNTs. Open and filled circles are for SI and SII SWNTs. (c) Binding energy Kataura plots for M SWNTs.

dence of the effective mass of the carriers, as is discussed below. Also, the family spread of E_{bd} is increased by curvature effects, as will be seen below. In Fig. 8(c), we show the exciton binding energy for M SWNTs. We use $E_{iiL}^M(A_2^0)$ and $E_{iiH}^M(A_2^0)$ to label the A_2^0 exciton states in the lower and higher energy branch for E_{ii} transitions in the energy Kataura plot. The cutting lines for E_{iiL}^M and E_{iiH}^M states are outside and inside the 2D BZ, respectively. It is seen that similar $(2n+m)$-family patterns are present in the exciton binding energy of M and S SWNTs, respectively, shown in Figs. 8(c) and 8(b). Moreover, although the exciton binding energy in M SWNTs is generally small, it can exceed 0.1 eV for some SWNTs with small d_t, especially for $E_{11H}^M(A_2^0)$ states. By considering that the exciton binding energy can now be measured by experiments,[14,31,40] the chirality dependence shown in Fig. 8 is expected to provide important information for interpreting experiments.

Figures 8(b) and 8(c) show that the exciton binding energy in a S SWNT with a small d_t can be as large as 1 eV, while that in a M SWNT is smaller than 0.2 eV. The difference arises from the different electron screening effect in S and M SWNTs. The free electrons in M SWNTs, i.e., electrons in two metallic bands crossing the Fermi level, give rise to different dielectric functions in M SWNTs than those in S SWNTs. By considering the electron screening effect, the bare Coulomb interaction $V(\mathbf{q})$ is replaced by a screened Coulomb interaction $V(\mathbf{q})/\epsilon(\mathbf{q})$. As we have mentioned, $l_k < 2/d_t$ and thus one cutting line is sufficient to describe E_{ii} states. Therefore, when we discuss the properties of the ex-
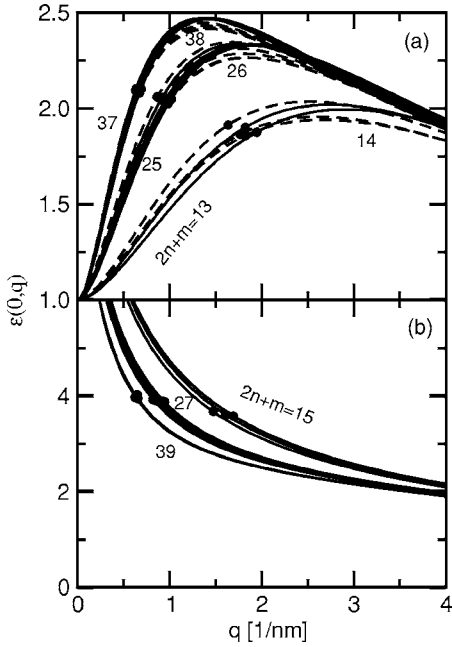
FIG. 9. The dielectric function $\epsilon(0,q)$ for (a) S SWNTs and (b) M SWNTs. The integers denote $(2n+m)$ values (a) 13, 14, 25, 26, 37, and 38 and (b) 15, 27, and 39. The dots indicate the position with $q=1/d_t$. In (a) solid and dashed lines are for SI and SII SWNTs.

FIG. 10. The exciton binding energy for $E_{33}(A_2^0)$ and $E_{44}(A_2^0)$ states with 1.0 nm$<d_t<$1.6 nm. Open and filled circles are for SI and SII SWNTs for $E_{33}(A_2^0)$ states, and open and filled squares are for SI and SII SWNTs for $E_{44}(A_2^0)$ states. For SI SWNTs, (n,m) =(9,7) and (10, 8) SWNTs with families $2n+m=25$ and 28, respectively, have the same binding energies for $E_{33}(A_2^0)$ and $E_{44}(A_2^0)$ states.

citon binding energy, we only need to consider the dielectric function with $\mathbf{q}\equiv(\mu,q)=(0,q)$, i.e., $\epsilon(0,q)$. Figures 9(a) and 9(b) show $\epsilon(0,q)$ for S and M SWNTs, respectively. $\epsilon(0,q)$ is an even function of q and thus in Fig. 9 we show $\epsilon(0,q)$ with $q\geqslant0$. In Fig. 9(a) for S SWNTs, we show ϵ for the SWNTs with families $2n+m=13$, 14, 25, 26, 37, and 38 and in Fig. 9(b) for M SWNTs, we show ϵ for the SWNTs with families $2n+m=15$, 27, and 39. The tube diameter d_t increases from about 0.55, 1.10, to about 1.50 nm for the family $2n+m$ value from 13 (14), 25 (26), to 37 (38) and d_t increases from about 0.62, 1.12 nm to about 1.58 nm for the family $2n+m$ value from 15, 27 to 39. By increasing d_t, the energy gap of S SWNTs decreases and thus the screening effect tends to increase, which can be seen from Fig. 9. For M SWNTS, by increasing d_t the confinement of the free electrons is relaxed from 1D to 2D and thus the screening effect tends to decrease, which can also be seen from Fig. 9, where we use dark dots to indicate the positions with $q=1/d_t$. By considering that $l_k<2/d_t$, the screening effect in the range of $|q|<1/d_t$ is most important in determining the exciton binding energy. For a S SWNT, Fig. 9(a) shows that ϵ decreases from a value around 2.0 to 1.0 when q decreases from $1/d_t$ to 0. That means that, for q approaching to 0, the screening effect decreases and it completely disappears at $q=0$. On the other hand, for a M SWNT, Fig. 9(b) shows that ϵ increases to infinity with q decreasing from $1/d_t$ to 0. That means, for q approaching to 0 the screening effect increases and the Coulomb interaction is completely screened at $q=0$. Since the Coulomb interaction is screened efficiently in M SWNTs by π electrons, the exciton binding energy becomes small. The opposite behavior in $\epsilon(0,q)$ for S and M SWNTs arises from the free electrons near the Fermi level in M
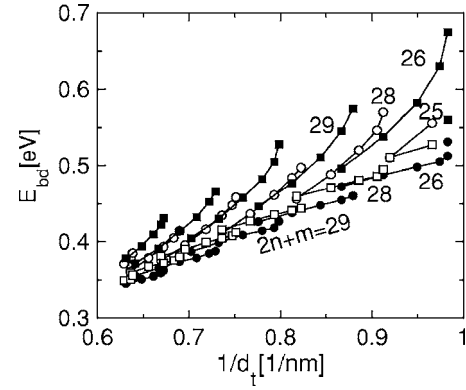
SWNTs, which are not present for S SWNTs. If we remove the contribution from the metallic bands in the dielectric function calculation, the curves in Fig. 9(b) become similar to those in Fig. 9(a), and the binding energies for M SWNTs show similar values as those for S SWNTs.

Raman experiments often probe signals from E_{22}^S, E_{33}^S, E_{44}^S, and E_{11}^M transitions.[6,7,41] Therefore, it is interesting to see what happens for the exciton binding energy for $E_{33}(A_2^0)$ and $E_{44}(A_2^0)$ states of S SWNTs. In Fig. 10, we plot the exciton binding for $E_{33}(A_2^0)$ and $E_{44}(A_2^0)$ states with d_t in the range of 1.0 nm$<d_t<$1.6 nm, corresponding to excitation energies $E_{ii}\leqslant3.0$ eV. We note that for the same d_t value, the exciton binding energies for $E_{33}(A_2^0)$ and $E_{44}(A_2^0)$ states generally have a bit larger values than for $E_{22}(A_2^0)$ states. From Fig. 10, we can see that the exciton binding energies for $E_{33}(A_2^0)$ and $E_{44}(A_2^0)$ states also show a tube type dependence and family behavior. As we see from Figs. 8 and 10, the family branch arrangement in the two figures is different. In Fig. 10, the binding energies for $E_{44}(A_2^0)$ and $E_{33}(A_2^0)$ states give rise to lower and higher branches in SI SWNTs, while it becomes the opposite in SII SWNTs. The different binding energy branch arrangement in Figs. 10 and 8 remains to be confirmed by future experiments.

In the two-photon fluorescence experiments, by comparison of the two-photon excitation energy to the emission energy, the relevant energy difference for the $E_{11}(A_2^1)$ and $E_{11}(A_2^0)$ states can be obtained.[13,14] We calculate the excitation energy difference for the A_2^1 and A_2^0 states. The results are shown in Fig. 11 for $E_{11}(A_2^1)-E_{11}(A_2^0)$ and $E_{22}(A_2^1)-E_{22}(A_2^0)$. We can see that the energy difference has a strong d_t dependence, but almost no tube type dependence nor family behavior. The excitation energy difference for $E_{ii}(A_2^1)$ and $E_{ii}(A_2^0)$ equals the exciton binding difference between them. We find that the exciton binding energies for $E_{11}(A_2^1)$ and $E_{22}(A_2^1)$ have a similar tube type and family pattern dependence as those for $E_{11}(A_2^0)$ and $E_{22}(A_2^0)$ shown in Fig. 8(a). Thus, the tube type dependence and family pat-
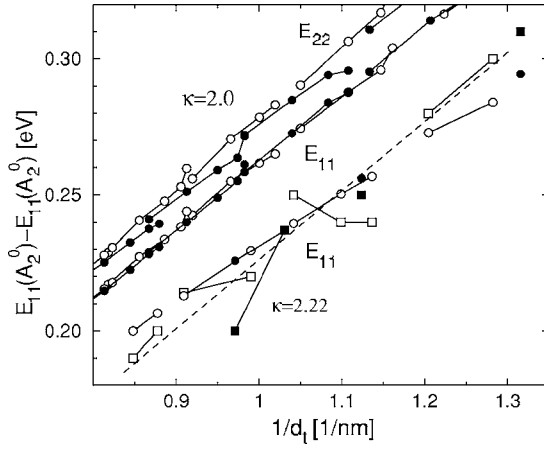
FIG. 11. The excitation energy differences $E_{11}(A_2^1) - E_{11}(A_2^0)$ and $E_{22}(A_2^1) - E_{22}(A_2^0)$ (upper). Open and filled circles are calculated data for SI and SII SWNTs. Open and filled squares are experimental data by Dukovic *et al.* (Ref. 42) for SI and SII SWNTs. The dashed line is a fitted relationship between $E_{11}(A_2^1) - E_{11}(A_2^0)$ and $1/d_t$ for the experimental data. The theoretical data around the dashed line are calculated only for $E_{11}(A_2^1) - E_{11}(A_2^0)$ with $\kappa = 2.22$.

terns are almost canceled by the energy differences $E_{22}(A_2^1) - E_{22}(A_2^0)$ and $E_{11}(A_2^1) - E_{11}(A_2^0)$ with $\kappa = 2$ (upper part). Figure 11 also shows that $E_{22}(A_2^1) - E_{22}(A_2^0)$ and $E_{11}(A_2^1) - E_{11}(A_2^0)$ have values similar to each other. Recently, Dukovic *et al.* have measured $E_{11}(A_2^1) - E_{11}(A_2^0)$ for 13 SWNTs.[42] We fit their experimental data as shown in Fig. 11 by changing the κ value to $\kappa = 2.22$ (lower part). It is seen that the calculation is consistent with the measurements. From the $E_{11}(A_2^1) - E_{11}(A_2^0)$ ratio between our result with $\kappa = 2$ and the experimental one for a (9, 5) SWNT and using the scaling law $E_{bd} \approx (1/\kappa)^{1.4}$ found by Perebeinos *et al.*,[23] which is consistent with the present result (see also Fig. 13), we obtain the fitted κ value (2.22) for the samples. There are also other experiments measuring the energy differences for several SWNTs. The experimentally measured $E_{11}(A_2^1) - E_{11}(A_2^0)$ for (8,3), (6,5), and (7,5) SWNTs by Wang *et al.*[13] are 0.30, 0.31, and 0.28 eV, respectively, and the experimentally measured energy differences for (6,4), (9,1), (8,3), (6,5), (7,5), and (9,4) SWNTs by Maultzcsh *et al.*[14] are 0.325, 0.315, 0.295, 0.285, 0.240, and 0.280 eV. Our calculated values for (6,4), (9,1), (8,3), (6,5), (7,5), and (9,4) SWNTs by using $\kappa = 2.22$ are 0.314, 0.291, 0.284, 0.344, 0.272, and 0.250 eV. Our calculated values are consistent with their measurements.[13,14] We note that the ordering of values for (8,3), (6,5), (7,5), and (9,4) SWNTs by our calculations are consistent with the measurements by Dukovic *et al.*,[42] while it is different from the measurements by Maultzcsh *et al.*[14]

B. Excitation energy shift by the environment

In Eq. (6) we introduce κ to include the screening effect from the environment. Thus, by studying the excitation energy dependence on κ, we can see how the environmental effect shifts the excitation energy. By changing the κ value from 3 to 2, we calculate the excitation energy and get the energy shift $\Delta E_{ii}(A_2^0) = E_{ii}(A_2^0)|_{\kappa=2} - E_{ii}(A_2^0)|_{\kappa=3}$. The results
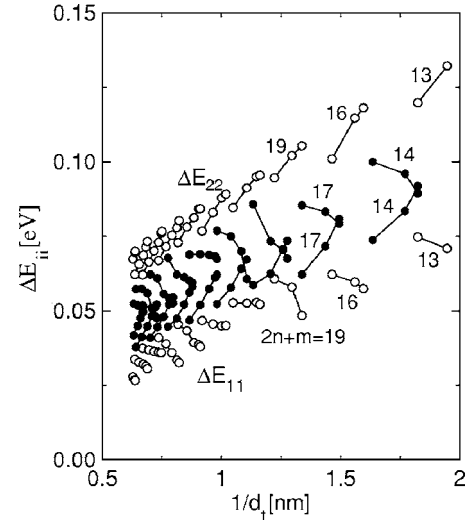

FIG. 12. The $E_{11}(A_2^0)$ and $E_{22}(A_2^0)$ excitation energy shifts by κ changing from 3 to 2, $\Delta E_{ii} = E_{ii}|_{\kappa=2} - E_{ii}|_{\kappa=3}$. Open and filled circles are for SI and SII SWNTs.

are shown in Fig. 12. It is interesting to see that there are also tube type and $(2n+m)$-family dependences predicted for ΔE_{ii}. However, by comparing the results of Fig. 12 with those of Figs. 4 and 8, we find that the tube type dependence here is different from that in l_k and in the binding energy. That is, for ΔE_{11} within the same $2n+m$ family, the value of ΔE_{11} increases with increasing chiral angle θ for SI SWNTs while it decreases with θ for SII SWNTs. For ΔE_{22} within the same $2n+m$ family, in contrast, the value of ΔE_{22} decreases with θ for SI SWNTs while it increases with θ for SII SWNTs. These tube type and chiral angle dependences are consistent with those observed by recent experiments.[43]

Experimental measurements[44,45] show that the excitation energy shift ΔE_{ii} by the environment is generally up to 80 meV, which is consistent with Fig. 13. In Fig. 13, we show the excitation energy dependence on κ with (solid line) and without (dashed line) including the electron screening effect for $E_{11}(A_2^0)$ and $E_{22}(A_2^0)$ states for a (6,5) SWNT. It is seen that without considering the electron screening effect,
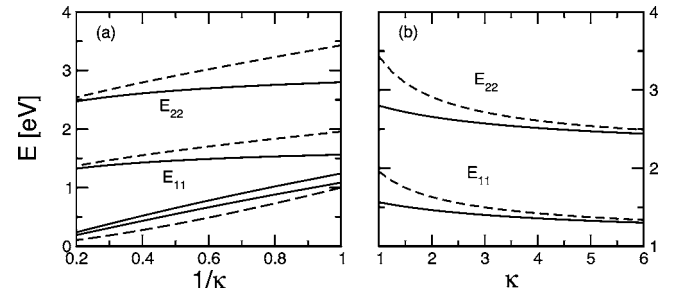

FIG. 13. The excitation energy dependence on κ for states $E_{11}(A_2^0)$ and $E_{22}(A_2^0)$ for (6,5) SWNTs. Solid and dashed lines are with and without considering the π electron screening effect, respectively. (a) Excitation energy vs $1/\kappa$. The three curves below E_{11} are exciton binding energies for $E_{22}(A_2^0)$ and $E_{11}(A_2^0)$, and the function $E = (1/\kappa)^{1.4}$ from top to bottom, respectively. (b) Excitation energy vs κ.
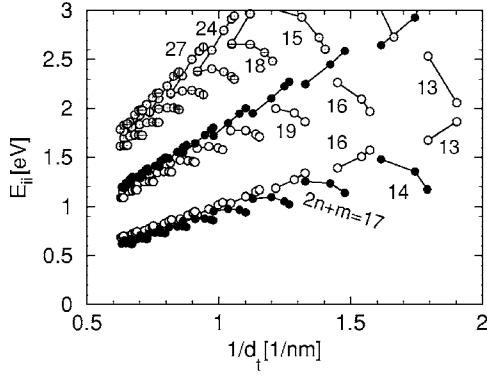
FIG. 14. The excitation energy Kataura plot based on the ETB model for $E_{11}^S(A_2^0)$ and $E_{22}^S(A_2^0)$ for S SWNTs and $E_{11}^M(A_2^0)$ for M SWNTs. Open and filled circles are for SI and SII SWNTs, respectively, and crossed circles are for M SWNTs.

E_{ii} is approximately linearly dependent on $1/\kappa$. The screening effect will bend the line, reducing the energy shift, especially for the small κ region, e.g., $\kappa < 2$. The bending effect arises from the fact that the screening effect by the environment generally provides a dielectric constant, independent of the wave vector $\mathbf{q}$, while the dielectric function $\epsilon(0,q)$ from the electron screening effect is a function of q.[20] In Fig. 13(a), we also show the exciton binding energy vs $1/\kappa$. It is seen that for both E_{11} and E_{22} states, the binding energy approximately scales as[23] $(1/\kappa)^{1.4}$. In view of the experiments, the environmental dielectric constants can be varied from close to 1 to a large value by putting the SWNT samples in air or water. When κ is large, e.g., $\kappa > 5$, Fig. 13(b) shows that the value of the excitation energy turns out to be the same with and without the electron screening effect and it becomes independent of κ. The reason is that the Coulomb interaction becomes very small in the case of large κ and the excitation energy approaches the single-particle energy. Figure 13(b) shows that without the electron screening effect, the excitation energy variation can exceed 0.5 eV as κ increases from 1 to infinity, while the variation is decreased due to the electron screening effect in the SWNT.

C. Excitation energy Kataura plot based on the ETB model

As we have already pointed out, the simple TB model is not sufficient to describe the large family spread in the Ka-
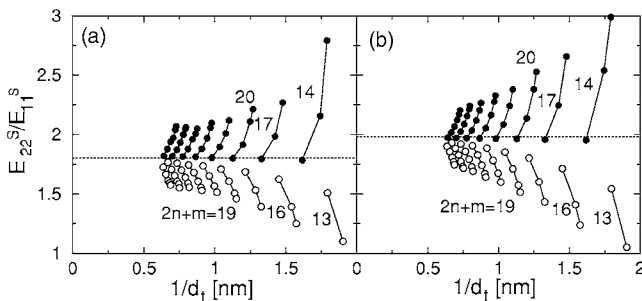

FIG. 15. The excitation energy ratio E_{22}^S/E_{11}^S for A_2^0 states based on the ETB model for S SWNTs with 0.5 nm $< d_t <$ 1.6 nm. Open and filled circles are for SI and SII SWNTs, respectively. (a) and (b) are the results with and without Coulomb interaction. The dashed lines are used to indicate the values for the average ratio.

taura plot. Thus, we calculate the excitation energy again by the ETB, as shown in Fig. 14. In Fig. 14 we plot the data for the $E_{11}^S(A_2^0)$ and $E_{22}^S(A_2^0)$ states for S SWNTs and the $E_{11}^M(A_2^0)$ states for M SWNTs. The large family spread appears, which again is consistent with previous calculations[2,3] and experiments.[5,9]

In Fig. 15, we show the energy E_{22}^S/E_{11}^S ratio for A_2^0 states for S SWNTs with $0.5 < d_t < 1.6$ nm. The average ratio in this diameter range is about (a) 1.8 and (b) 2.0 with and without Coulomb interaction, respectively. The average ratio of E_{22}^S/E_{11}^S is approximately the ratio for the SII SWNTs with chiral angle $\theta \sim 30°$, which is located around the dashed line in Fig. 15. Figure 15 also shows a tube type dependence and family patterns. Moreover, the many-body effect decreases the energy ratio for all SII SWNTs and for most of the SI SWNTs.

To understand whether single-particle spectra or many-body effects contribute to the large family spread in the excitation Kataura plot, we plot the excitation energy E_{11}, the self-energy correction to the quasiparticle energy Σ, the exciton binding energy E_{bd}, and the energy correction to the single-particle energy $\Sigma - E_{bd}$ in the same figure (Fig. 16). It is seen that Σ tends to increase the family spread of the single-particle spectra, while this increased spread is almost canceled by the spread from the exciton binding energy, leading to a weak family spread in the net energy correction ($\Sigma - E_{bd}$) to the single-particle energy. Thus, the large family spread in E_{11} is given by the single-particle spectra. The curvature effect and the C-C bond length optimization in small d_t SWNTs contribute to the large family spread for the single-particle spectra.[2] It is known that the logarithmic correction from the effect of the Coulomb interaction on the dispersion of 2D graphene is not fully canceled by the exciton binding energy and leads to a logarithmic energy correction $E^{\log}$ as given by[3,10]

$$E^{\log} = 0.55(2p/3d_t)\log[3/(2p/3d_t)]. \tag{28}$$

In Fig. 16, we plot $E^{\log}$ with $p=1$ as a dashed line. It is seen that our energy correction $\Sigma - E_{bd}$ follows this logarithmic
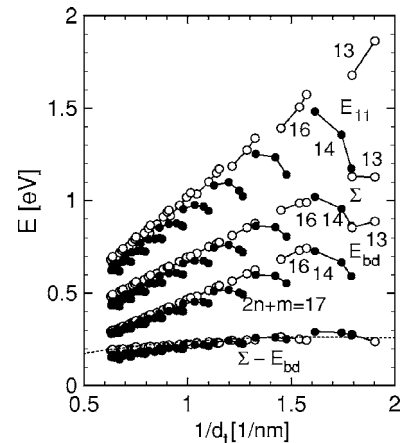

FIG. 16. The excitation energy E_{11}, self-energy Σ, binding energy E_{bd}, and energy corrections $\Sigma - E_{bd}$ based on ETB for $E_{11}(A_2^0)$ states. Open and filled circles are for SI and SII SWNTs. The dashed line is calculated by Eq. (28) with $p=1$.

behavior well. Comparing Fig. 16 with Fig. 8, we find that E_{bd} shows a similar tube type and family behavior by the simple and extended TB models. However, the C-C bond length optimization modifies the detailed family patterns by bending the branches for SII SWNTs, thereby increasing the family spread.

V. DISCUSSIONS AND SUMMARY

Recently, calculations based on an *ab initio* many-electron Green's function approach to electron-hole interaction effects on the optical spectra of small-diameter SWNTs were reported.[11] For (8,0) tubes in vacuum, the excitation energies for $E_{11}(A_2^0)$ and $E_{22}(A_2^0)$ states are found to be 1.55 and 1.80 eV, respectively. The corresponding energy ratio is $E_{22}/E_{11}=1.16$. The binding energies for $E_{11}(A_2^0)$ and $E_{22}(A_2^0)$ states are found to about 1.00 and 0.86 eV, respectively. For comparison, we calculated the excitation and binding energies based on the ETB model for (8,0) tubes by taking $\kappa=1.0$. The calculated excitation energies for the $E_{11}(A_2^0)$ and $E_{22}(A_2^0)$ states are 1.57 and 2.10 eV, respectively, and correspondingly $E_{22}/E_{11}=1.33$. The calculated binding energies for the $E_{11}(A_2^0)$ and $E_{22}(A_2^0)$ states are 1.21 and 1.10 eV, respectively. It is seen that our results are consistent with the *ab initio* results. Since the nanotube screening is mainly from the electrons near the Fermi level, inclusion of only π electrons is expected to explain well the nanotube screening, which is confirmed by the above comparison between our results and those coming from *ab initio* results. We should mention that generally the $E_{22}(A_2^0)$ states have a larger binding energy than the $E_{11}(A_2^0)$ states. However, for SI SWNTs with a small d_t, the $E_{11}(A_2^0)$ states can have a larger binding energy than the $E_{22}(A_2^0)$ states as can be seen from Fig. 8(b).

In addition to the electron screening, we have also considered the screening from the surrounding media by introducing a dielectric constant κ. With κ going from 1 to infinity, the exciton binding energy for a S SWNT varies from a finite value to zero. Since the quasiparticle and binding energies vary with κ in a similar way, the excitation energy varies over a small energy range with κ from 1 to infinity, as we have seen from Fig. 13. Actually, in both the simple TB and ETB models we found that the two lowest transition energies for a SWNT generally vary in an energy range smaller than 0.2 eV with κ from 1 to infinity.

Figure 2 indicates that there is an energy splitting between the bright exciton state $E_{11}(A_2^0)$ and the dark exciton state $E_{11}(A_1^0)$. The splitting energy is determined by the difference between the matrix element of the BS equation for the $E_{11}(A_2^0)$ state and that for the $E_{11}(A_1^0)$ state. The matrix element difference is expressed by $2[2K^x(\mathbf{k}',-\mathbf{k};0)-K^d(\mathbf{k}',-\mathbf{k};0)]$. By taking $\kappa=1$, we calculated a splitting energy for a (10,0) tube. Without the π electron screening the splitting energy is about 14 meV and the dark exciton has a lower energy. With the π electron screening, the splitting increases to be about 25 meV, which is consistent with the *ab initio* calculation for a (10,0) tube in vacuum, i.e., 29 meV. Since K^x and K^d are the unscreened and screened Coulomb interactions, respectively, the screening effect in-
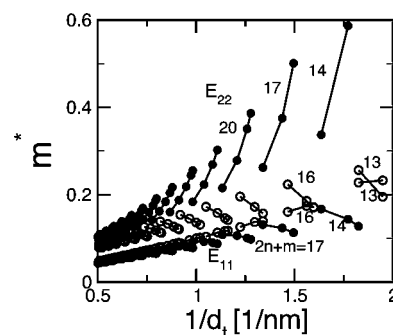

FIG. 17. The effective mass for the first and second transitions for S SWNTs based on the ETB model. Open and filled circles are for SI and SII SWNTs.

creases the splitting energy by decreasing the K^d value.

The family behavior in the excitation energy, binding energy, and wave function size arises from the same reason, that is, from the trigonal warping effect.[46] The curvature effect will modify the family patterns, especially for the single-particle spectra. The first van Hove singularities (vHSs) for SI and SII SWNTs are outside (along the KM line) and inside (along the ΓK line) of the first BZ of graphene, while it becomes opposite for the second vHSs. Around the K point, the energy bands of graphene are generally more flat inside the BZ than outside the BZ. Thus, the effective mass m^* is generally larger inside and smaller outside the BZ. Therefore, m^* exhibits a tube type dependence as shown in Fig. 17. This tube type dependence for m^* will in turn bring in a similar tube type dependence for the wave function size and in the exciton binding energy [see Figs. 4 and 8(b)]. For example, for $E_{22}(A_2^0)$ states, m^* is larger for SII SWNTs than for SI SWNTs and thus l_k and the exciton binding energy are longer and larger, respectively, for SII SWNTs than for SI SWNTs. The effective mass also shows family patterns as is seen in Fig. 17 and in turn similar family patterns appear in the wave function size and in the exciton binding energy [see Figs. 4 and 8(b)].

In summary, we have studied the excitation properties in SWNTs by solving the BS equation within the STB and ETB models. The exciton wave functions along the SWNT axis and circumference directions are studied and a circumference moment is found for $E_{12}(A)$ excitons. The wave function extended length l_k in k space is found to be smaller than the cutting line spacing $2/d_t$. Moreover, an SI and SII tube type dependence and family behavior are found in the wave function length, excitation energy, binding energy, and excitation energy shift by the environment. The electron screening effect is found to be essential for explaining the small energy shift by the environment and the different exciton binding energies for S and M SWNTs. The energy differences between the first and second exciton levels are calculated and the results for the E_{11} transition agree well with the experimental measurements. The origin of the family patterns are understood from the trigonal warping effect and the tube curvature effects.

ACKNOWLEDGMENTS

[1] R. Saito, G. Dresselhaus, and M. S. Dresselhaus, *Physical Properties of Carbon Nanotubes* (Imperial College Press, London, 1998).

[2] Ge. G. Samsonidze, R. Saito, N. Kobayashi, A. Grüneis, J. Jiang, A. Jorio, S. G. Chou, G. Dresselhaus, and M. S. Dresselhaus, Appl. Phys. Lett. **85**, 5703 (2004).

[3] A. Jorio, C. Fantini, M. A. Pimenta, R. B. Capaz, Ge. G. Samsonidze, G. Dresselhaus, M. S. Dresselhaus, J. Jiang, N. Kobayashi, A. Grüneis, and R. Saito, Phys. Rev. B **71**, 075401 (2005).

[4] M. J. O'Connell, S. M. Bachilo, X. B. Huffman, V. C. Moore, M. S. Strano, E. H. Haroz, K. L. Rialon, P. J. Boul, W. H. Noon, C. Kittrell, J. Ma, R. H. Hauge, R. B. Weisman, and R. E. Smalley, Science **297**, 593 (2002).

[5] S. M. Bachilo, M. S. Strano, C. Kittrell, R. H. Hauge, R. E. Smalley, and R. B. Weisman, Science **298**, 2361 (2002).

[6] A. Jorio, A. G. Souza Filho, G. Dresselhaus, M. S. Dresselhaus, R. Saito, J. H. Hafner, C. M. Lieber, F. M. Matinaga, M. S. S. Dantas, and M. A. Pimenta, Phys. Rev. B **63**, 245416 (2001).

[7] M. S. Dresselhaus, Ge. G. Samsonidze, S. G. Chou, G. Dresselhaus, J. Jiang, R. Saito, and A. Jorio, Physica E (Amsterdam) **29**, 443 (2005).

[8] M. S. Dresselhaus, G. Dresselhaus, R. Saito, and A. Jorio, Phys. Rep. **409**, 47 (2005).

[9] C. Fantini, A. Jorio, M. Souza, M. S. Strano, M. S. Dresselhaus, and M. A. Pimenta, Phys. Rev. Lett. **93**, 147406 (2004).

[10] C. L. Kane and E. J. Mele, Phys. Rev. Lett. **90**, 207401 (2003).

[11] C. D. Spataru, Sohrab Ismail-Beigi, Lorin X. Benedict, and Steven G. Louie, Phys. Rev. Lett. **92**, 077402 (2004).

[12] C. D. Spataru, S. Ismail-Beigi, L. X. Benedict, and S. G. Louie, Appl. Phys. A: Mater. Sci. Process. **78**, 1129 (2004).

[13] F. Wang, G. Dukovic, L. E. Brus, and T. F. Heinz, Science **308**, 838 (2005).

[14] J. Maultzsch, R. Pomraenke, S. Reich, E. Chang, D. Prezzi, A. Ruini, E. Molinari, M. S. Strano, C. Thomsen, and C. Lienau, Phys. Rev. B **72**, 241402(R) (2005).

[15] S. G. Chou, F. P. Filho, J. Jiang, R. Saito, D. Nezich, H. B. Ribeiro, A. Jorio, M. A. Pimenta, Ge. G. Samsonidze, A. P. Santos, M. Zheng, G. B. Onoa, E. D. Semke, G. Dresselhaus, and M. S. Dresselhaus, Phys. Rev. Lett. **94**, 127402 (2005); F. Plentz, H. B. Ribeiro, A. Jorio, M. S. Strano, and M. A. Pimenta, *ibid.* **95**, 247401 (2005).

[16] S. G. Chou, M. F. DeCamp, J. Jiang, Ge. G. Samsonidze, E. B. Barros, F. Plentz, A. Jorio, M. Zheng, G. B. Onoa, E. D. Semke, A. Tokmakoff, R. Saito, G. Dresselhaus, and M. S. Dresselhaus, Phys. Rev. B **72**, 195415 (2005).

[17] L. Marty, E. Adam, L. Albert, R. Doyon, D. Menard, and R. Martel, Phys. Rev. Lett. **96**, 136803 (2006).

[18] L. Huang and T. D. Krauss, Phys. Rev. Lett. **96**, 057407 (2006).

[19] Y. Z. Ma, L. Valkunas, S. L. Dexheimer, S. M. Bachilo, and G. R. Fleming, Phys. Rev. Lett. **94**, 157402 (2005).

[20] T. Ando, J. Phys. Soc. Jpn. **66**, 1066 (1997).

[21] E. Chang, G. Bussi, A. Ruini, and E. Molinari, Phys. Rev. Lett. **92**, 196401 (2004).

[22] C. D. Spataru, S. Ismail-Beigi, R. B. Capaz, and S. G. Louie, Phys. Rev. Lett. **95**, 247402 (2005).

[23] V. Perebeinos, J. Tersoff, and P. Avouris, Phys. Rev. Lett. **92**, 257402 (2004).

[24] V. Perebeinos, J. Tersoff, and P. Avouris, Nano Lett. **5**, 2495 (2005).

[25] T. G. Pedersen, Phys. Rev. B **67**, 073401 (2003).

[26] H. Zhao and S. Mazumdar, Synth. Met. **155**, 250 (2005).

[27] T. Ando, J. Phys. Soc. Jpn. **74**, 777 (2005).

[28] T. Ando, J. Phys. Soc. Jpn. **73**, 3351 (2004).

[29] J. Jiang, R. Saito, K. Sato, J. S. Park, Ge. G. Samsonidze, A. Jorio, G. Dresselhaus, and M. S. Dresselhaus, Phys. Rev. B **75**, 035405 (2007).

[30] M. Rohlfing and S. G. Louie, Phys. Rev. B **62**, 4927 (2000).

[31] Z. Wang, H. Pedrosa, T. Krauss, and L. Rothberg, Phys. Rev. Lett. **96**, 047403 (2006).

[32] N. E. Brener, Phys. Rev. B **12**, 1487 (1975).

[33] Ge. G. Samsonidze, R. Saito, A. Jorio, M. A. Pimenta, A. G. Souza Filho, A. Grüneis, G. Dresselhaus, and M. S. Dresselhaus, J. Nanosci. Nanotechnol. **3**, 431 (2003).

[34] R. Saito, K. Sato, Y. Oyama, J. Jiang, Ge. G. Samsonidze, G. Dresselhaus, and M. S. Dresselhaus, Phys. Rev. B **72**, 153413 (2005).

[35] E. B. Barros, R. B. Capaz, A. Jorio, Ge. G. Samsonidze, A. G. Souza Filho, S. Ismail-Beigi, C. D. Spataru, S. G. Louie, G. Dresselhaus, and M. S. Dresselhaus, Phys. Rev. B **73**, 241406(R) (2005); E. B. Barros, A. Jorio, Ge. G. Samsonidze, R. B. Capaz, A. G. Souza Filho, J. Mendez Filho, G. Dresselhaus, and M. S. Dresselhaus, Phys. Rep. **431**, 261 (2006).

[36] C. C. J. Roothaan, J. Chem. Phys. **19**, 1445 (1951).

[37] D. Porezag, Th. Frauenheim, Th. Köhler, G. Seifert, and R. Kaschner, Phys. Rev. B **51**, 12947 (1995).

[38] Y. Miyauchi, M. Oba, and S. Maruyama, Phys. Rev. B **74**, 205440 (2006).

[39] S. Uryu and T. Ando, Phys. Rev. B **74**, 155411 (2006).

[40] Y. Z. Ma, L. Valkunas, S. M. Bachilo, and G. R. Fleming, J. Phys. Chem. B **109**, 15671 (2005).

[41] P. T. Araujo, S. K. Doorn, S. Kilina, S. Tretiak, E. Einarsson, S. Maruyama, H. Chacham, M. A. Pimenta, and A. Jorio, Phys. Rev. Lett. (to be published).

[42] G. Dukovic, F. Wang, D. Song, M. Y. Sfeir, T. F. Heinz, and L. E. Brus, Nano Lett. **5**, 2314 (2005).

[43] Y. Ohno, S. Iwasaki, Y. Murakami, S. Kishimoto, S. Maruyama, and T. Mizutani, Phys. Rev. B **73**, 235427 (2006).

[44] H. Son, Y. Hori, S. G. Chou, D. Nezich, Ge. G. Samsonidze, G. Dresselhaus, M. S. Dresselhaus, and E. Barros, Appl. Phys. Lett. **85**, 4744 (2004).

[45] C. Fantini, A. Jorio, M. Souza, M. S. Strano, M. S. Dresselhaus, and M. A. Pimenta, Phys. Rev. Lett. **93**, 147406 (2004).

[46] R. Saito, G. Dresselhaus, and M. S. Dresselhaus, Phys. Rev. B **61**, 2981 (2000).